

PAPER • OPEN ACCESS

An adaptive deep-coupled GNSS/INS navigation system with hybrid pre-filter processing

To cite this article: Mouyan Wu *et al* 2018 *Meas. Sci. Technol.* **29** 025103

View the [article online](#) for updates and enhancements.

You may also like

- [On the use of pre-filters in quadrupole mass spectrometers](#)
C Trajber, M Simon and M Csatos
- [\(Invited, Digital Presentation\) Photocurrent Detection of Cooperative Exciton Quantum Interference in Nanocrystal Thin Films](#)
Hirokazu Tahara and Yoshihiko Kanemitsu
- [Focus on X-ray Beams with High Coherence](#)
Ian Robinson, Gerhard Gruebel and Simon Mochrie

An adaptive deep-coupled GNSS/INS navigation system with hybrid pre-filter processing

Mouyan Wu[✉], Jicheng Ding¹, Lin Zhao¹, Yingyao Kang and Zhibin Luo

College of Automation, Harbin Engineering University, Harbin 150001, People's Republic of China

E-mail: aaron.heu@163.com and zhaolin@hrbeu.edu.cn

Received 16 June 2017, revised 24 October 2017

Accepted for publication 27 October 2017

Published 19 January 2018



Abstract

The deep-coupling of a global navigation satellite system (GNSS) with an inertial navigation system (INS) can provide accurate and reliable navigation information. There are several kinds of deeply-coupled structures. These can be divided mainly into coherent and non-coherent pre-filter based structures, which have their own strong advantages and disadvantages, especially in accuracy and robustness. In this paper, the existing pre-filters of the deeply-coupled structures are analyzed and modified to improve them firstly. Then, an adaptive GNSS/INS deeply-coupled algorithm with hybrid pre-filters processing is proposed to combine the advantages of coherent and non-coherent structures. An adaptive hysteresis controller is designed to implement the hybrid pre-filters processing strategy. The simulation and vehicle test results show that the adaptive deeply-coupled algorithm with hybrid pre-filters processing can effectively improve navigation accuracy and robustness, especially in a GNSS-challenged environment.

Keywords: deeply-coupled, pre-filter, hybrid, accuracy, robustness

(Some figures may appear in colour only in the online journal)

1. Introduction

A traditional global navigation satellite system (GNSS) receiver tracks each satellite independently and each channel does not permit information sharing among other channels. The performance between dynamic and noise suppression is a tradeoff for the tracking loop bandwidth [1, 2]. The integrated navigation system of GNSSs and inertial navigation systems (INSs) was developed to improve the accuracy and robustness of the system [3–6]. The deeply-coupled (also called ultra-tight) navigation system is one of these effective integrated systems. Some recent researches on deeply-coupled navigation systems include the acquisition and loop control

algorithms [7, 8], the fusion methods of the GNSS and INS [9, 10] and other related fields [11, 12].

Generally, deeply-coupled navigation systems can be classified as having a centralized filtering architecture or a federated filtering architecture [13–16]. However, the centralized filtering architecture suffers from a high computation burden and complex relationship between in-phase/quadrature-phase (I/Q) correlator outputs and INS errors for hardware implementation [15]. Thus, only the federated filtering architecture will be discussed in the following sections of this paper.

In the federated architecture, the I/Q measurements are firstly pre-processed by a series of pre-filters and then the integrated navigation filter is used to process the output of the pre-filters and to restrict the INS errors. The INS navigation solutions and GNSS ephemerides are used to control the numerically controlled oscillators (NCOs) of code and carrier [16].

The pre-filter is a key technology of the deeply-coupled navigation system, which can be mainly divided into two

¹ Authors to whom any correspondence should be addressed.



Original content from this work may be used under the terms of the [Creative Commons Attribution 3.0 licence](https://creativecommons.org/licenses/by/3.0/). Any further distribution of this work must maintain attribution to the author(s) and the title of the work, journal citation and DOI.

categories, coherent and non-coherent [17, 18]. The coherent algorithm inputs the GNSS accumulated correlator outputs, i.e. the I_s and Q_s , directly to the Kalman filter as measurements. The non-coherent algorithm firstly passes the I_s and Q_s through code and carrier discriminator functions, similar to those used in conventional GNSS signal tracking. The coherent algorithm bypasses the discriminators, avoiding the introduction of unmodeled nonlinear in the measurement inputs to the Kalman filter, and can reach a less noisy tracking performance than the non-coherent algorithm. However, it is unsuited to applications that require operation under low signal-to-noise environments as both code and carrier-frequency tracking can be maintained at a lower carrier power-to-noise density ratio (C/N_0) than carrier-phase tracking. On the contrary, the non-coherent algorithm can work well whether there is sufficient C/N_0 to track carrier phase because the code discriminator function is independent of the carrier phase. This enables the non-coherent algorithm to maintain tracking in weaker signal environments than the coherent algorithm.

In order to improve the accuracy and robustness of the system, an adaptive deeply-coupled GNSS/INS navigation system with hybrid pre-filters processing is proposed in this paper. The existing pre-filter algorithms are analyzed and modified to overcome their shortcomings firstly. Then, a hybrid-based pre-filter processing strategy is introduced. An adaptive hysteresis controller is designed to implement the hybrid pre-filters processing strategy. Finally, the simulation and vehicle tests are conducted to assess the system's performance.

2. Hybrid-based adaptive pre-filter processing

2.1. Analysis of the existing pre-filter algorithms

There are three main structures of pre-filter, as summarized in [14]. The existing coherent pre-filter algorithm (option #1 in [14]) follows closely the filter implementation proposed in [19, 20]. The correlator outputs shown in (1) and (2) are used directly as the measurements of the Kalman filter,

$$I = A \cdot \frac{\sin(\pi \cdot \delta f \cdot T)}{\pi \cdot \delta f \cdot T} \cdot D \cdot R(\delta\tau + \Delta_k) \cdot \cos(\delta\bar{\Phi}) + n_I \quad (1)$$

$$Q = A \cdot \frac{\sin(\pi \cdot \delta f \cdot T)}{\pi \cdot \delta f \cdot T} \cdot D \cdot R(\delta\tau + \Delta_k) \cdot \sin(\delta\bar{\Phi}) + n_Q \quad (2)$$

where A represents the accumulated amplitude, T is the integration period, D is the navigation data bits of the GNSS, $R(\cdot)$ is the autocorrelation function of the ranging code, $\delta\tau$ is the code phase bias between the local replica code and the incoming signals and δf is the frequency error (Hz) between the local replica frequency and the incoming signals. Δ_k is the correlator spacing for early, prompt and delay code, where $k = -1, 0, 1$. n_I and n_Q are the noise of I and Q . $\delta\bar{\Phi}$ is the average phase error over the integration interval, which can be written as

$$\delta\bar{\Phi} = \delta\phi_0 + \frac{1}{2}\delta f_0 T + \frac{1}{6}\delta a_0 T^2 \quad (3)$$

where $\delta\phi_0$ and δf_0 indicate the initial phase error and the initial carrier frequency error at the start of the integration interval, respectively, and δa_0 is the carrier phase acceleration error.

The system model for this implementation is written as follows:

$$\frac{d}{dt} \begin{bmatrix} A \\ \delta\tau \\ \delta\varphi_0 \\ \delta f_0 \\ \delta a_0 \end{bmatrix} = \begin{bmatrix} 0 & 0 & 0 & 0 & 0 \\ 0 & 0 & 0 & \beta & 0 \\ 0 & 0 & 0 & 1 & 0 \\ 0 & 0 & 0 & 0 & 1 \\ 0 & 0 & 0 & 0 & 0 \end{bmatrix} \cdot \begin{bmatrix} A \\ \delta\tau \\ \delta\varphi_0 \\ \delta f_0 \\ \delta a_0 \end{bmatrix} + \begin{bmatrix} 1 & 0 & 0 & 0 & 0 \\ 0 & 1 & \alpha & 0 & 0 \\ 0 & 0 & 1 & 0 & 0 \\ 0 & 0 & 0 & 1 & 0 \\ 0 & 0 & 0 & 0 & 1 \end{bmatrix} \cdot \begin{bmatrix} w_A \\ w_{mp} \\ w_{clock} \\ w_{drift} \\ w_{accel} \end{bmatrix} \quad (4)$$

where β converts units of rad/s into units of chips per second. w_A is the process noise for the amplitude; w_{mp} is the process noise for the code phase error to account for code multipath effects; w_{clock} is the process noise for the clock bias; w_{drift} is the process noise for the clock drift; and w_{accel} is the process noise for the phase acceleration (which is related to the receiver dynamics).

For the first existing non-coherent pre-filter algorithm (option #2 in [14]), the system model is the same as option #1, whereas the measurements are changed to the output of the carrier discriminator function and combination of I and Q , which are shown as follows:

$$Z_1 = \delta\bar{\phi} = \arctan(Q_P/I_P) \quad (5)$$

$$Z_2 = \sqrt{I^2 + Q^2} = A \cdot \frac{\sin(\pi \cdot \delta f \cdot T)}{\pi \cdot \delta f \cdot T} D \cdot R(\delta\tau + \Delta_k). \quad (6)$$

The relationship between states and measurements in option #1 would be nonlinear, and option #2 has the problem of the measurement noise correlation originating from the nonlinear combination of I_s and Q_s data. Besides, the signal amplitude item in option #1 may suffer the initial value setting problem and cause a convergence speed of the filter in some cases like a sudden change of the signal amplitude. Conversely, we can exclude the signal amplitude A from the system model and estimate it separately and quickly using the C/N_0 estimator. This change can avoid the initial signal amplitude value setting of the filter, speed up the convergence speed of the filter, and also reduce the dimensions of the Kalman filter. The signal amplitude item in option #2 is not needed and can also be excluded from the state vector.

The system model of the second existing non-coherent pre-filter algorithm (Option #3 in [14]) is shown as follows:

$$\frac{d}{dt} \begin{bmatrix} A \\ \delta\rho_0 \\ \delta\dot{\rho}_0 \\ \delta\ddot{\rho}_0 \\ \delta I_{on} \end{bmatrix} = \begin{bmatrix} 0 & 0 & 0 & 0 & 0 \\ 0 & 0 & 1 & 0 & 0 \\ 0 & 0 & 0 & 1 & 0 \\ 0 & 0 & 0 & 0 & 0 \\ 0 & 0 & 0 & 0 & 0 \end{bmatrix} \cdot \begin{bmatrix} A \\ \delta\rho_0 \\ \delta\dot{\rho}_0 \\ \delta\ddot{\rho}_0 \\ \delta I_{on} \end{bmatrix} + \begin{bmatrix} 1 & 0 & 0 \\ 0 & 0 & 0 \\ 0 & 0 & 0 \\ 0 & 1 & 0 \\ 0 & 0 & 1 \end{bmatrix} \cdot \begin{bmatrix} w_A \\ w_{accel} \\ w_{I_{on}} \end{bmatrix} \quad (7)$$

where A is the normalized signal amplitude, $\delta\rho_0$ is the pseudorange error, $\delta\dot{\rho}_0$ is the pseudorange error rate, $\delta\ddot{\rho}_0$ is the pseudorange error accelerator, and δI_{on} is the ionospheric error.

The accuracy of the pseudorange information and ionospheric correction error information (especially in single-point operation) are usually not accurate enough for carrier phase tracking in vector-tracking and deeply-coupled mode. Therefore, option #3 is not appropriate for carrier tracking, as concluded by [14].

2.2. Modification and improvement of the pre-filter algorithms

2.2.1. Coherent pre-filter algorithm. Firstly, we exclude the signal amplitude A from the system model and estimate it separately using the C/N_0 estimator. The detail of A in (1) and (2) can be further described as

$$A = \sqrt{2 \cdot (c/n_0) \cdot T \cdot \sigma_{\text{IQ}}} \quad (8)$$

where c/n_0 represents the carrier power-to-noise density (unit of Hz), T is the integration interval, and σ_{IQ} is the standard deviation of noise.

Then, the state vector and the system model of the coherent pre-filter algorithm can be modified as

$$\begin{aligned} \mathbf{X}_{\text{coh}} &= [\delta\tau, \delta\phi_0, \delta f_0, \delta a_0]^T \quad (9) \\ \frac{d}{dt} \begin{bmatrix} \delta\tau \\ \delta\phi_0 \\ \delta f_0 \\ \delta a_0 \end{bmatrix} &= \begin{bmatrix} 0 & 0 & \beta & 0 \\ 0 & 0 & 1 & 0 \\ 0 & 0 & 0 & 1 \\ 0 & 0 & 0 & 0 \end{bmatrix} \cdot \begin{bmatrix} \delta\tau \\ \delta\phi_0 \\ \delta f_0 \\ \delta a_0 \end{bmatrix} \\ &+ \begin{bmatrix} 1 & \alpha & 0 & 0 \\ 0 & 1 & 0 & 0 \\ 0 & 0 & 1 & 0 \\ 0 & 0 & 0 & 1 \end{bmatrix} \cdot \begin{bmatrix} w_{\text{mp}} \\ w_{\text{clock}} \\ w_{\text{drift}} \\ w_{\text{accel}} \end{bmatrix}. \quad (10) \end{aligned}$$

It is known that in the coherent pre-filter algorithm, the GNSS accumulated correlator outputs I_s and Q_s directly to the Kalman filter as measurements in the coherent algorithm. The six-measurement model with measurements in-phase and quadra-phase prompt, early and late (I_P , Q_P , I_E , Q_E , I_L and Q_L) are used as the pre-filter algorithm, shown as

$$\mathbf{Z}_{\text{coh}} = \mathbf{A} \cdot \mathbf{D} \cdot \mathbf{h}(\mathbf{X}_{\text{coh}}) + \mathbf{n}_{\text{IQ}} \quad (11)$$

$$\begin{bmatrix} I_E \\ Q_E \\ I_P \\ Q_P \\ I_L \\ Q_L \end{bmatrix} = \begin{bmatrix} A \cdot \text{sinc}(\delta f \cdot T) \cdot D \cdot R(\delta\tau + \Delta_{-1}) \cdot \cos(\delta\bar{\Phi}) \\ A \cdot \text{sinc}(\delta f \cdot T) \cdot D \cdot R(\delta\tau + \Delta_{-1}) \cdot \sin(\delta\bar{\Phi}) \\ A \cdot \text{sinc}(\delta f \cdot T) \cdot D \cdot R(\delta\tau + \Delta_0) \cdot \cos(\delta\bar{\Phi}) \\ A \cdot \text{sinc}(\delta f \cdot T) \cdot D \cdot R(\delta\tau + \Delta_0) \cdot \sin(\delta\bar{\Phi}) \\ A \cdot \text{sinc}(\delta f \cdot T) \cdot D \cdot R(\delta\tau + \Delta_{+1}) \cdot \cos(\delta\bar{\Phi}) \\ A \cdot \text{sinc}(\delta f \cdot T) \cdot D \cdot R(\delta\tau + \Delta_{+1}) \cdot \sin(\delta\bar{\Phi}) \end{bmatrix} + \begin{bmatrix} n_{I_E} \\ n_{Q_E} \\ n_{I_P} \\ n_{Q_P} \\ n_{I_L} \\ n_{Q_L} \end{bmatrix}. \quad (12)$$

Besides, the ideal autocorrelation function $R(\cdot)$ is not differentiable and also not realistic when the input RF signal has passed through a band-pass filter [21–23]. A more realistic autocorrelation function, which is a 6th order polynomial approximation of $R(\cdot)$, is used in the local filter as follows:

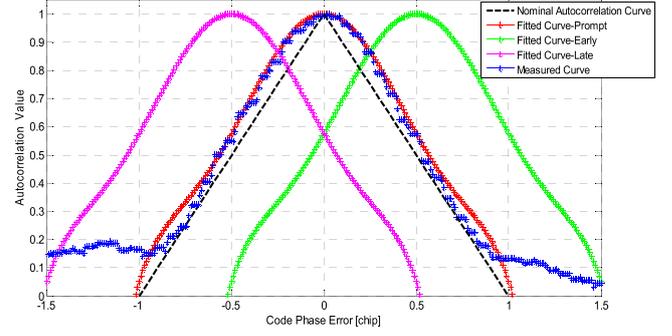


Figure 1. The fitting curve of 6th order polynomial approximation for code autocorrelation function.

$$R(\tau) \approx x_6\tau^6 + x_5\tau^5 + x_4\tau^4 + x_3\tau^3 + x_2\tau^2 + x_1\tau + x_0. \quad (13)$$

As shown in figure 1, the blue curve denotes the actual measured curve coming from the GNSS IF signal collector, the black curve is the nominal autocorrelation curve and the red curve denotes the fitting curve of the 6th order polynomial approximation (prompt branch). The other two curves are fitting curves of the 6th order polynomial approximation for early and late branches, respectively. It can be seen that the fitting curves of the 6th order polynomial approximation are more realistic than the nominal autocorrelation curve, especially when the code phase error is small. Although the approximation needs more computation than the nominal autocorrelation function, it can get a better accuracy of the autocorrelation function.

To solve the nonlinear problem and get a higher filter accuracy, a five-degree cubature Kalman filter (5th-CKF) for the coherent pre-filter is proposed. The 5th-CKF uses a series of cubature points to propagate the *a priori* and *a posteriori* statistical characteristics. The core of the CKF is a cubature transformation based on the spherical-radial rule [24, 25].

The five-degree spherical-radial cubature rule's points and weights can be calculated as follows:

$$\begin{cases} \xi_0 = 0 \\ \xi_{1i} = \sqrt{n+2}e_i \\ \xi_{2i} = -\sqrt{n+2}e_i \\ \xi_{3i} = \sqrt{n+2}s_i^+ \\ \xi_{4i} = -\sqrt{n+2}s_i^+ \\ \xi_{5i} = \sqrt{n+2}s_i^- \\ \xi_{6i} = -\sqrt{n+2}s_i^- \end{cases}, \begin{cases} w_0 = \frac{2}{n+2} \\ w_1 = \frac{4-n}{2(n+2)^2} (i=1, 2, \dots, n) \\ w_2 = \frac{1}{(n+2)^2} (i=1, 2, \dots, \frac{n(n-1)}{2}) \end{cases} \quad (14)$$

where e_i denotes a unit vector in the direction of coordinate axis i . s_i^+ and s_i^- are described as

$$\begin{cases} s_i^+ = \sqrt{1/2}(e_j + e_l) \\ s_i^- = \sqrt{1/2}(e_j - e_l) \end{cases} \quad (15)$$

$(i=1, 2, \dots, \frac{n(n-1)}{2}, \quad j < l, \quad j, l=1, 2, \dots, n).$

The coherent pre-filter based on 5th-CKF works as follows.

2.2.1.1. Time update. The posterior probability density of \mathbf{x}_{k-1} is known in previous update $\mathbf{p}(x_{k-1}) = N(\mathbf{x}_{k-1|k-1}, \mathbf{P}_{k-1|k-1})$. The Cholesky decomposition of $\mathbf{P}_{k-1|k-1}$ is calculated as follows:

$$\mathbf{P}_{k-1|k-1} = \mathbf{S}_{k-1|k-1} \mathbf{S}_{k-1|k-1}^T. \quad (16)$$

The cubature points are calculated as

$$\begin{cases} \mathbf{X}_{0,k-1|k-1} = \mathbf{S}_{k-1|k-1} \xi_0 + \hat{\mathbf{x}}_{k-1|k-1} \\ \mathbf{X}_{ri,k-1|k-1} = \mathbf{S}_{k-1|k-1} \xi_{ri} + \hat{\mathbf{x}}_{k-1|k-1}, \quad . \\ (r = 1, 2, \dots, 6; \quad i = 1, 2, \dots, n) \end{cases} \quad (17)$$

Then, the sample points are obtained by propagating the above cubature points through the system model in (10), as follows:

$$\begin{cases} \mathbf{X}_{0,k|k-1}^* = \mathbf{F}(\mathbf{X}_{0,k-1|k-1}) \\ \mathbf{X}_{ri,k|k-1}^* = \mathbf{F}(\mathbf{X}_{ri,k-1|k-1}), \\ (r = 1, 2, \dots, 6; \quad i = 1, 2, \dots, n) \end{cases} \quad (18)$$

where \mathbf{F} is the system matrix of the coherent pre-filter.

One-step state prediction $\hat{\mathbf{x}}_{k|k-1}$ is then obtained by the weighted linear combination of sample points, as follows:

$$\begin{aligned} \hat{\mathbf{x}}_{k|k-1} = w_0 \mathbf{X}_{0,k|k-1}^* + w_1 \sum_{i=1}^n \sum_{r=1}^2 \mathbf{X}_{ri,k|k-1}^* \\ + w_2 \sum_{i=1}^{n(n-1)/2} \sum_{r=3}^6 \mathbf{X}_{ri,k|k-1}^*. \end{aligned} \quad (19)$$

One-step state prediction error covariance $\mathbf{P}_{k|k-1}$ is updated as follows:

$$\begin{aligned} \mathbf{P}_{k|k-1} = w_0 \mathbf{X}_{0,k|k-1}^* \mathbf{X}_{0,k|k-1}^{*T} \\ + w_1 \sum_{i=1}^n \sum_{r=1}^2 \left(\mathbf{X}_{ri,k|k-1}^* \mathbf{X}_{ri,k|k-1}^{*T} \right) \\ + w_2 \sum_{i=1}^{n(n-1)/2} \sum_{r=3}^6 \left(\mathbf{X}_{ri,k|k-1}^* \mathbf{X}_{ri,k|k-1}^{*T} \right) \\ - \hat{\mathbf{x}}_{k|k-1} \hat{\mathbf{x}}_{k|k-1}^T + \mathbf{Q}_{k-1}. \end{aligned} \quad (20)$$

2.2.1.2. Measurement update. The Cholesky decomposition of $\mathbf{P}_{k|k-1}$ is calculated as follows:

$$\mathbf{P}_{k|k-1} = \mathbf{S}_{k|k-1} \mathbf{S}_{k|k-1}^T. \quad (21)$$

The cubature points are calculated as

$$\begin{cases} \mathbf{X}_{0,k|k-1} = \mathbf{S}_{k|k-1} \xi_0 + \hat{\mathbf{x}}_{k|k-1} \\ \mathbf{X}_{ri,k|k-1} = \mathbf{S}_{k|k-1} \xi_{ri} + \hat{\mathbf{x}}_{k|k-1}, \quad . \\ (r = 1, 2, \dots, 6; \quad i = 1, 2, \dots, n) \end{cases} \quad (22)$$

Then, the sample points are obtained by propagating the above cubature points through the measurement equation in (11), as follows:

$$\begin{cases} \mathbf{Z}_{0,k|k-1}^* = \mathbf{A} \cdot \mathbf{D} \cdot h(\mathbf{X}_{0,k|k-1}) \\ \mathbf{Z}_{ri,k|k-1}^* = \mathbf{A} \cdot \mathbf{D} \cdot h(\mathbf{X}_{ri,k|k-1}), \quad . \\ (r = 1, 2, \dots, 6; \quad i = 1, 2, \dots, n) \end{cases} \quad (23)$$

One-step measurement prediction $\hat{\mathbf{z}}_{k|k-1}$ is then obtained by the weighted linear combination of sample points as follows:

$$\begin{aligned} \hat{\mathbf{z}}_{k|k-1} = w_0 \mathbf{Z}_{0,k|k-1}^* + w_1 \sum_{i=1}^n \sum_{r=1}^2 \mathbf{Z}_{ri,k|k-1}^* \\ + w_2 \sum_{i=1}^{n(n-1)/2} \sum_{r=3}^6 \mathbf{Z}_{ri,k|k-1}^*. \end{aligned} \quad (24)$$

The auto-correlation covariance matrix $\mathbf{P}_{zz,k|k-1}$ is obtained as

$$\begin{aligned} \mathbf{P}_{zz,k|k-1} = w_0 \mathbf{Z}_{0,k|k-1}^* \mathbf{Z}_{0,k|k-1}^{*T} \\ + w_1 \sum_{i=1}^n \sum_{r=1}^2 \left(\mathbf{Z}_{ri,k|k-1}^* \mathbf{Z}_{ri,k|k-1}^{*T} \right) \\ + w_2 \sum_{i=1}^{n(n-1)/2} \sum_{r=3}^6 \left(\mathbf{Z}_{ri,k|k-1}^* \mathbf{Z}_{ri,k|k-1}^{*T} \right) \\ - \hat{\mathbf{z}}_{k|k-1} \hat{\mathbf{z}}_{k|k-1}^T + \mathbf{R}_k. \end{aligned} \quad (25)$$

The cross-correlation covariance matrix $\mathbf{P}_{xz,k|k-1}$ is calculated as follows:

$$\begin{aligned} \mathbf{P}_{xz,k|k-1} = w_0 \mathbf{X}_{0,k|k-1}^* \mathbf{Z}_{0,k|k-1}^{*T} \\ + w_1 \sum_{i=1}^n \sum_{r=1}^2 \left(\mathbf{X}_{ri,k|k-1}^* \mathbf{Z}_{ri,k|k-1}^{*T} \right) \\ + w_2 \sum_{i=1}^{n(n-1)/2} \sum_{r=3}^6 \left(\mathbf{X}_{ri,k|k-1}^* \mathbf{Z}_{ri,k|k-1}^{*T} \right) - \hat{\mathbf{x}}_{k|k-1} \hat{\mathbf{z}}_{k|k-1}^T. \end{aligned} \quad (26)$$

The Kalman filter gain is calculated as follows:

$$\mathbf{W}_k = \mathbf{P}_{xz,k|k-1} \mathbf{P}_{zz,k|k-1}^{-1}. \quad (27)$$

The state estimation $\hat{\mathbf{x}}_{k|k}$ is calculated as follows:

$$\hat{\mathbf{x}}_{k|k} = \hat{\mathbf{x}}_{k|k-1} + \mathbf{W}_k (\mathbf{z}_k - \hat{\mathbf{z}}_{k|k-1}). \quad (28)$$

The state estimation error covariance $\mathbf{P}_{k|k}$ is calculated as follows:

$$\mathbf{P}_{k|k} = \mathbf{P}_{k|k-1} - \mathbf{W}_k \mathbf{P}_{zz,k|k-1} \mathbf{W}_k^T \quad (29)$$

where $\hat{\mathbf{x}}_{k|k}$ and $\mathbf{P}_{k|k}$ are used in the next iteration.

2.2.2. Non-coherent pre-filter algorithm. For the non-coherent pre-filter algorithm, we simplify the state vector and the system model as

$$\mathbf{X}_{\text{nonCoh}} = [\delta\tau, \delta f, \delta a]^T \quad (30)$$

$$\begin{aligned} \frac{d}{dt} \begin{bmatrix} \delta\tau \\ \delta f \\ \delta a_0 \end{bmatrix} = \begin{bmatrix} 0 & 0 & 0 \\ 0 & 0 & 1 \\ 0 & 0 & 0 \end{bmatrix} \cdot \begin{bmatrix} \delta\tau \\ \delta f \\ \delta a_0 \end{bmatrix} \\ + \begin{bmatrix} 1 & 0 & 0 \\ 0 & 1 & 0 \\ 0 & 0 & 1 \end{bmatrix} \cdot \begin{bmatrix} w_{\text{mp}} \\ w_{\text{drift}} \\ w_{\text{accel}} \end{bmatrix}. \end{aligned} \quad (31)$$

Meanwhile, the measurements are designed as

$$\mathbf{Z}_{\text{nonCoh}} = [\delta\tau, \delta f]^T \quad (32)$$

$$\begin{bmatrix} \delta\tau \\ \delta f \end{bmatrix} = \begin{bmatrix} (1 - \Delta) \cdot \frac{\sqrt{I_E^2 + Q_E^2} - \sqrt{I_L^2 + Q_L^2}}{\sqrt{I_E^2 + Q_E^2} + \sqrt{I_L^2 + Q_L^2}} \\ \frac{\arctan 2(P_{\text{cross}} P_{\text{dot}})}{2\pi \cdot [t(n) - t(n-1)]} \end{bmatrix} + \begin{bmatrix} n_\tau \\ n_f \end{bmatrix} \quad (33)$$

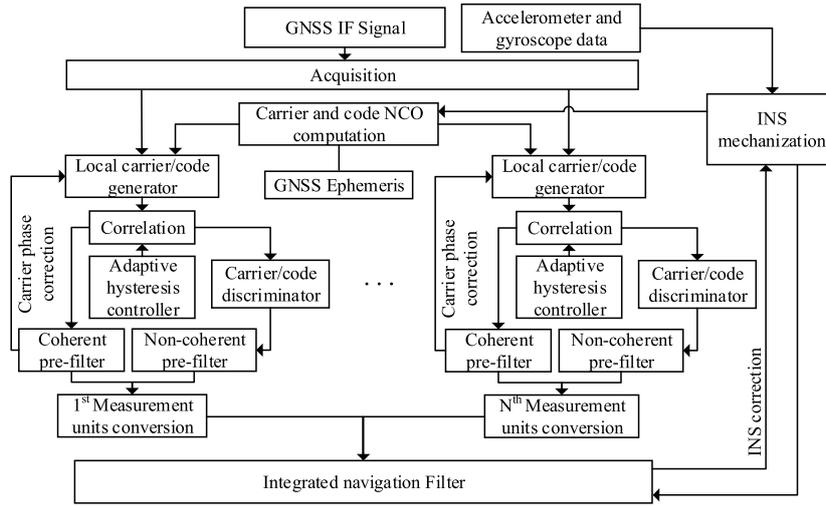


Figure 2. Adaptive robust deeply-coupled architecture with hybrid pre-filters processing.

where $P_{\text{cross}} = I_P(n-1)Q_P(n) - Q_P(n-1)I_P(n)$ and $P_{\text{dot}} = I_P(n-1)I_P(n) + Q_P(n-1)Q_P(n)$.

The modification can be summarized as follows.

First, the signal amplitude and carrier phase error state are excluded from the system model shown in (31). Then, we replace the carrier phase discriminator by a carrier frequency discriminator to estimate the carrier frequency error and its derivatives. The output of the code phase discriminator is used to observe the code errors, which can be seen in (33). Besides, it can be seen from (31) that the code state and carrier state are modeled as independent of each other.

The reason is that the noise characteristics of I and Q almost fulfill an additive white Gaussian noise (AWGN) assumption, so the measurement noise of the coherent pre-filter algorithm would be independent. However, the discriminators' outputs or the nonlinear combinations of I_s and Q_s data are considered as measurement information in the non-coherent pre-filter algorithm, so any two kinds of the measurement noise would not be independent, which violates the *a priori* condition of the Kalman filter [26]. Thus, we use the carrier frequency discriminator to keep carrier tracking in order to get a robustness performance. The carrier phase tracking is mainly maintained by traditional carrier phase discriminator in (5), but only the carrier frequency tracking would be maintained in a lower C/N_0 environment. In addition, the independent modelling of the code and carrier state would further reduce the influence of measurement correlation.

2.3. Hybrid-based adaptive pre-filter strategy

In order to improve the accuracy and robustness of the system, this paper proposes a hybrid-based adaptive pre-filter strategy according to the level of C/N_0 . The diagram of the proposed system is shown in figure 2.

The adaptive hysteresis controller is designed to implement an automatic switch between coherent and non-coherent modes. First, the C/N_0 estimation is calculated by the method of narrow-to-wideband power ratio (NWPR) [27]. The prompt I and Q samples over the accumulation interval τ are divided

into M intervals. These samples are then used to calculate a narrowband power, P_{nb} , over the whole accumulation interval and a wideband power, P_{wb} , over the interval τ/M , then summed over τ . These power estimates are described as

$$P_{\text{wb}} = \sum_i^M (I_{\text{Pi}}^2 + Q_{\text{Pi}}^2) \quad (34)$$

$$P_{\text{nb}} = \left(\sum_i^M I_{\text{Pi}}^2 \right)^2 + \left(\sum_i^M Q_{\text{Pi}}^2 \right)^2 \quad (35)$$

where $I_{\text{Pi}} = \sqrt{2(c/n_0)\tau/M} \cos\varphi + \omega_{\text{IPi}}$ and $Q_{\text{Pi}} = \sqrt{2(c/n_0)\tau/M} \sin\varphi + \omega_{\text{QPi}}$. The ω_{IPi} and ω_{QPi} are normalized random noise samples from a zero-mean unit variance normal Gaussian distribution.

The narrow-to-wide power ratio, P_{nw} , is simply the ratio of the two power measurements. However, to reduce the noise, the measurement is averaged over K iterations. Thus,

$$\mu_P = \frac{1}{K} \sum_{k=1}^K P_{\text{nw}}. \quad (36)$$

Finally, the measured carrier power-to-noise density (Hz) is derived as a function of the power ratio measurement, shown as

$$c/n_0 = \frac{M}{\tau} \frac{\mu_P - 1}{M - \mu_P}. \quad (37)$$

Besides, the standard deviation of the can be calculated as follows:

$$\sigma(c/n_0) = \frac{M}{\tau} \frac{M-1}{(M-\mu_P)^2} \frac{\sigma(P_{\text{nw}})}{\sqrt{K}}. \quad (38)$$

Just as the C/N_0 value contains errors, a single threshold used to decide whether to switch the system mode or not may cause an abnormal frequency switch between the system's modes. To avoid this case, the adaptive hysteresis controller is designed based on the thought of a hysteresis-comparator circuit, which is shown in figure 3.

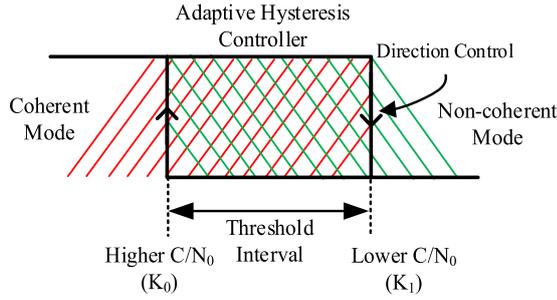


Figure 3. The adaptive hysteresis controller.

The controller is initialized in coherent mode and its control direction is set as down to allow the system to switch to non-coherent mode if the C/N_0 is lower to K_1 . The lower C/N_0 threshold is preset by the user (e.g. 35 dB-Hz) according to the coherent mode's better work range; the mode will change to coherent mode when the signal enhances again and exceeds the K_0 threshold.

The threshold interval is decided based on the standard deviation of the C/N_0 in (38) adaptively. A simple empirical value of the threshold interval can also be set (e.g. 1–3 dB-Hz) according to the empirical accuracy of the C/N_0 .

In the hybrid pre-filter's processing strategy, the integrated filter's measurements from the coherent pre-filter's output and non-coherent pre-filter's output are weighted by their noise covariance.

3. The design of the integrated navigation filter and NCO feedback control

3.1. Integrated navigation filter

The deep fusion of the combined GNSS and INS is accomplished by an integrated navigation filter. The states vector matrix \mathbf{X}_{nav} of the navigation filter is shown as

$$\mathbf{X}_{\text{nav}} = [\delta\varphi, \delta\lambda, \delta h, \delta v_e, \delta v_n, \delta v_u, \phi_x, \phi_y, \phi_z, \varepsilon_{bx}, \varepsilon_{by}, \varepsilon_{bz}, \nabla_x, \nabla_y, \nabla_z, \delta t_u, \delta t_f]^T. \quad (39)$$

The navigation filter estimates the errors of the user's three position, three velocity, three attitude, three gyroscope bias, three acceleration bias, clock bias and clock drift, respectively. The position error states are shown in a geodetic coordinate system. The velocity error states are shown in an east-north-up (ENU) frame.

The outputs of the hybrid pre-filters are taken as measurements for the integrated filter based on the errors of the replica code and carrier signals having relationships with the residual errors of the INS. The measurement of the integrated filter can be written as

$$\mathbf{Z}_{\text{nav}} = \begin{bmatrix} \delta\rho_1, \delta\rho_2, \dots, \delta\rho_n, \\ \delta\dot{\rho}_1, \delta\dot{\rho}_2, \dots, \delta\dot{\rho}_n \end{bmatrix}^T \quad (40)$$

where $\delta\rho_j$ and $\delta\dot{\rho}_j$ represent the pseudorange and pseudorange rate residual of j th satellite respectively. The measurement states are derived from the following equation:

$$\begin{bmatrix} \delta\rho \\ \delta\dot{\rho} \end{bmatrix} = \begin{bmatrix} \delta\tau \cdot \frac{c}{f_{\text{code}0}} \\ -\delta f \cdot \frac{c}{f_{\text{carrier}0}} \end{bmatrix} \quad (41)$$

where $\delta\tau$ and δf are the code phase error and carrier frequency error coming from the pre-filter, respectively. $f_{\text{carrier}0}$ and $f_{\text{code}0}$ denote the normalized carrier frequency and the ranging code chipping rate of GNSS signals. c is the speed of light.

The observation matrix given below in (42) is linearized at each measurement epoch to accommodate the error measurements from each channel:

$$\mathbf{H}_{\text{nav}} = \begin{bmatrix} s_x^1 & s_y^1 & s_z^1 & \mathbf{0}_{1 \times 12} & 1 & 0 \\ \vdots & \vdots & \vdots & \vdots & \vdots & \vdots \\ s_x^n & s_y^n & s_z^n & \mathbf{0}_{1 \times 12} & 1 & 0 \\ \mathbf{0}_{1 \times 3} & t_x^1 & t_y^1 & t_z^1 & \mathbf{0}_{1 \times 10} & 1 \\ \vdots & \vdots & \vdots & \vdots & \vdots & \vdots \\ \mathbf{0}_{1 \times 3} & t_x^n & t_y^n & t_z^n & \mathbf{0}_{1 \times 10} & 1 \end{bmatrix} \quad (42)$$

where $\begin{bmatrix} s_x^j \\ s_y^j \\ s_z^j \end{bmatrix}^T = \begin{bmatrix} e_x^j \\ e_y^j \\ e_z^j \end{bmatrix}^T \cdot \mathbf{C}_1 = \begin{bmatrix} e_x^j \\ e_y^j \\ e_z^j \end{bmatrix}^T$

$$\cdot \begin{bmatrix} -(R_n + h)\sin\varphi\cos\lambda & -(R_n + h)\cos\varphi\sin\lambda & \cos\varphi\cos\lambda \\ -(R_n + h)\sin\varphi\sin\lambda & (R_n + h)\cos\varphi\cos\lambda & \cos\varphi\sin\lambda \\ [R_n(1 - f^2) + h]\cos\varphi & 0 & \sin\varphi \end{bmatrix} \quad (43)$$

$$\begin{bmatrix} t_x^j \\ t_y^j \\ t_z^j \end{bmatrix}^T = \begin{bmatrix} e_x^j \\ e_y^j \\ e_z^j \end{bmatrix}^T \cdot \mathbf{C}_2 = \begin{bmatrix} e_x^j \\ e_y^j \\ e_z^j \end{bmatrix}^T \cdot \begin{bmatrix} -\sin\lambda & -\sin\varphi\cos\lambda & \cos\varphi\cos\lambda \\ \cos\lambda & -\sin\varphi\sin\lambda & \cos\varphi\sin\lambda \\ 0 & \cos\varphi & \sin\varphi \end{bmatrix}. \quad (44)$$

(φ, λ, h) are latitude, longitude and height over the ellipsoid, respectively. R_n is the radius of curvature in prime vertical and f is the degree of rotating ellipsoid. \mathbf{C}_1 and \mathbf{C}_2 are the transform matrixes of different coordinate systems for position and velocity, respectively. (e_x^j, e_y^j, e_z^j) are the components of the unit vector in the line-of-sight direction from the user navigation solutions to the j th GNSS satellite, which can be calculated as follows:

$$\begin{bmatrix} e_x^j \\ e_y^j \\ e_z^j \end{bmatrix} = \frac{\mathbf{X}_s^j - \mathbf{X}_u}{\|\mathbf{X}_s^j - \mathbf{X}_u\|} \quad (45)$$

where \mathbf{X}_u and \mathbf{X}^j are the position of the user and j th GNSS satellite, respectively.

3.2. NCO feedback control

The information feedback from the integrated navigation solution to the GNSS tracking loops forms another important part of the deep-coupling strategy. The corrected position and velocity states of the INS and the estimated clock states are converted into pseudoranges and range rates (Doppler

frequencies), and subsequently used to update the code and carrier NCOs.

The Doppler frequency for the j th tracking channel is predicted using (46) or can be a filtered version of its measurement:

$$\hat{f}_d^j = \frac{-\left(\hat{\nu}_u - \nu_s^j\right) \cdot \mathbf{e}^j + \hat{t}_f - t_f^j}{c} \cdot f_{\text{carrier}0} \quad (46)$$

where ν_s^j and t_f^j are the velocity vector and clock drift of the j th satellite. ν_u and \hat{t}_f are the user's velocity vector and clock drift. c is the speed of light.

Then, the carrier frequency is generated as

$$\begin{aligned} \hat{f}_{\text{carrier}}^j &= f_{\text{IF}} + \hat{f}_d^j + f_{\text{nco}} \\ &= f_{\text{IF}} - \frac{\left(\hat{\nu}_u - \nu_s^j\right) \cdot \mathbf{e}^j + \hat{t}_f - t_f^j}{c} \cdot f_{\text{carrier}0} + f_{\text{nco}} \end{aligned} \quad (47)$$

where f_{nco} is the carrier NCO correction item which is generated by the estimated carrier phase errors after passing the carrier loop filter.

The pseudorange for the j th tracking channel is predicted in (48):

$$\begin{aligned} \hat{\rho}^{j-} &= \|\mathbf{X}_u^- - \mathbf{X}_s^{j-}\| + \hat{t}_u^- \\ &= \sqrt{\left(\hat{x}_u^- - x_s^{j-}\right)^2 + \left(\hat{y}_u^- - y_s^{j-}\right)^2 + \left(\hat{z}_u^- - z_s^{j-}\right)^2} + \hat{t}_u^- \end{aligned} \quad (48)$$

where \hat{x}_u^- , \hat{y}_u^- , \hat{z}_u^- and \hat{t}_u^- are the user's predicted position and clock bias. \hat{x}_s^{j-} , \hat{y}_s^{j-} , \hat{z}_s^{j-} are the j th satellite's position. The code frequency is generated as

$$\hat{f}_{\text{code},k+1}^j = f_{\text{code}0} \cdot \left[1 - \frac{\hat{\rho}_{k+1}^{j-} - \hat{\rho}_k^{j-}}{c \cdot \tau_N} \right] \quad (49)$$

where τ_N is the code NCO update period. k denotes the k th update of the NCO.

Another way of generating the code frequency is by using the carrier-aided code structure, which can be expressed as follows:

$$\hat{f}_{\text{code}}^j = f_{\text{code}0} \cdot \left(1 + \hat{f}_d^j \cdot \frac{1}{f_{\text{carrier}0}} \right). \quad (50)$$

4. Results and discussions

4.1. Test description

Two sets of kinematic data were used to compare the performance of the adaptive deeply-coupled system with hybrid pre-filters processing. The first kinematic data were collected using a hardware GNSS simulator to assess the performance of the modified pre-filter algorithms. The second data were collected using vehicle tests to compare the performance of the adaptive deeply-coupled system with hybrid pre-filters processing (Hybrid-DC), the single coherent deeply-coupled method (Coherent-DC) and the single non-coherent deeply-coupled method (nonCoherent-DC) under a GNSS-challenged environment.

4.1.1. Simulation test description. The HWA-RNSS 7300 hardware simulator is a multiple constellation and frequency

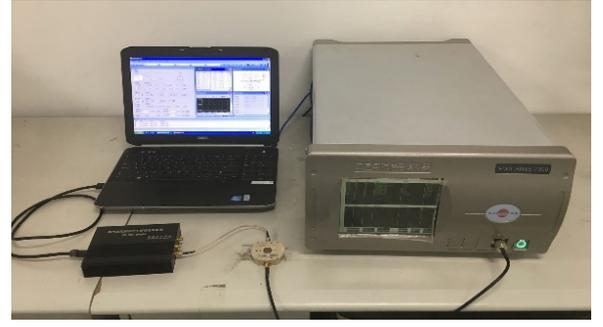


Figure 4. Data collection process with GNSS hardware simulator.

Table 1. Parameters defined in the system.

Parameter	Values
Gyro bias	1 deg h ⁻¹
Gyro noise density	0.004 deg/s/ $\sqrt{\text{Hz}}$
Accelerometer bias	0.005 mg
Accelerometer noise density	0.015 mg/ $\sqrt{\text{Hz}}$
GNSS sampling frequency	16.369 MHz
GNSS IF frequency	3.996 MHz
Coherent integration time	10 ms
Pre-filter period	100 Hz
Integrated filter period	10 Hz

GNSS simulator. The GNSS IF signal collector is a digital down converter that can receive GNSS signals through the GNSS antenna and then convert the high-frequency GNSS signals down to lower frequency signals. The data collection process is shown in figure 4.

In this simulation, the GPS L1 CA signals are simulated. The parameters of the simulated errors are set by the simulator and the known broadcast ephemeris which is stored in the simulator. The simulated errors include ionospheric error (using the Klobuchar model), tropospheric error (using the Hopfield model), the errors of broadcast orbits, the satellites' clock errors and relativistic effect. All these errors are preset by the simulator.

Besides, the true trajectory files from the hardware simulator are used to simulate the IMU information. Table 1 shows the detail parameters defined in the simulation test system.

4.1.2. Vehicle test description. The vehicle experiment platform consists of a GNSS IF signal collector, three inertial measurement units based on micro-electro-mechanical systems (MEMS-IMUs, only one used), two GNSS antenna (only one used), a splitter, a data logging computer and a reference system.

The experiment equipment is carried on a car, shown in figure 5(a). Figure 5(b) shows the data collection system. The GNSS IF signal collector is the same as above in figure 4. The IMU is manufactured by Inertial Labs. The reference system is shown in figures 5(c) and (d). Two ProPak6 receivers are used as rover receiver (configured as a GNSS/INS version) and base station receiver, respectively. The detail parameters defined in the vehicle test system are the same as the simulation test, which is shown in table 1.

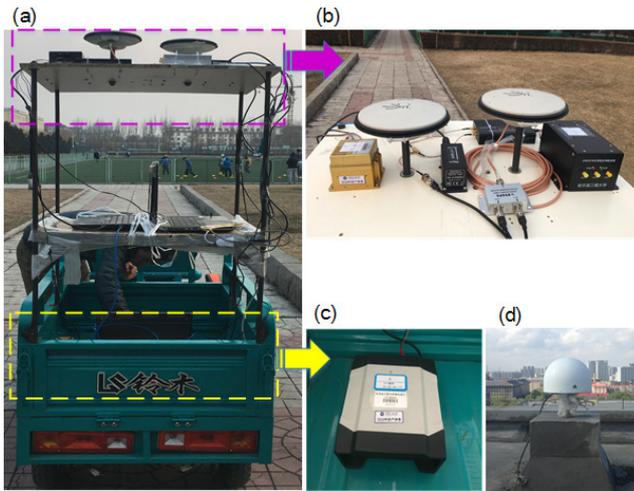


Figure 5. (a) Vehicle test car. (b) Data collection system. (c) Rover receiver. (d) Base station.

The proposed system works in single-point mode, while the reference system works in RTK mode and provides the precise position and velocity results as references to evaluate the performance of the proposed system.

4.2. Test results and discussions

4.2.1. Simulation test. During the test, the parameters of visible satellites and received signal power were set and shown in table 2.

The existing coherent pre-filter (*E-Coherent*), modified coherent pre-filter (*M-Coherent*), existing non-coherent pre-filter (*E-nonCoherent*) and modified non-coherent pre-filter (*M-nonCoherent*) methods are compared firstly for their tracking and navigation performance.

The carrier phase lock indicator (PLI) is used as the data analysis criterion. The PLI can be expressed as

$$PLI \approx \cos(2\delta\varphi). \tag{51}$$

The PLI is equal to 1 when the phase is perfectly locked and it is equal to -1 when the phase has no lock. We chose four satellites – SV2, SV10, SV17 and SV28 – to analyse the performance of the different algorithms.

Figure 6 shows the variation in carrier PLI of SV17 and SV28 using different pre-filter algorithms. Table 3 shows the PLI value statistics.

The Doppler frequency reference value from the hardware simulator is used to assess the tracking accuracy of Doppler frequency for the different algorithms. Figures 7–10 shows the Doppler frequency errors of SV17, SV28, SV2 and SV10 using different algorithms, respectively. Table 4 shows the Doppler frequency error statistics.

As shown in figure 6 and table 3, both of the coherent algorithms reach a better carrier phase lock than the non-coherent algorithms for high signal-to-noise signals. Besides, both of the *M-Coherent* and *M-nonCoherent* algorithms gain an improvement compared to the *E-Coherent* and *E-nonCoherent* algorithms, respectively. The tracking of SV2 and SV10 are lost for the coherent algorithms and only the carrier frequency for the non-coherent algorithms are shown in figures 9 and 10.

Table 2. Simulation conditions.

Visible satellites		SV# 2, 10, 17, 20, 23, 28 and 32
Velocity		5 m s ⁻¹
Simulation time		45s
C/N ₀	SV#2, 10	28 dB-Hz
	SV# others	45 dB-Hz

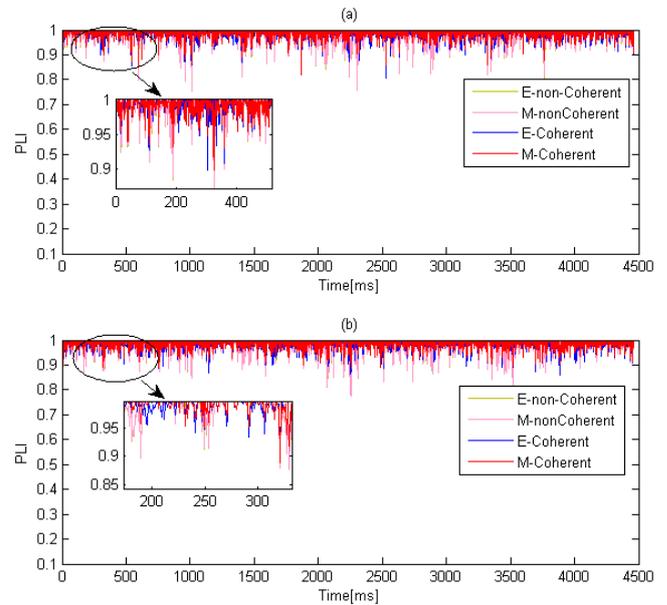


Figure 6. (a) The values of PLI for SV17. (b) The values of PLI for SV28.

Table 3. PLI value statistics.

Pre-filter method	PLI value (RMS) for different satellites			
	SV17	SV28	SV2	SV10
<i>E-Coherent</i>	0.9882	0.9882	/	/
<i>M-Coherent</i>	0.9895	0.9893	/	/
<i>E-nonCoherent</i>	0.9829	0.9825	/	/
<i>M-nonCoherent</i>	0.9830	0.9826	/	/

As shown in figures 7–10 and table 4, the Doppler frequency errors of the *M-Coherent* algorithm are reduced around 42% of the errors of *E-Coherent* algorithm for high signal-to-noise signals. Meanwhile, the errors of *M-nonCoherent* algorithm are reduced around 41% and 29% of the errors of the *E-nonCoherent* algorithm for high signal-to-noise signals and low signal-to-noise signals, respectively. In addition, both the coherent algorithms reach a better Doppler frequency tracking accuracy than the non-coherent algorithms for high signal-to-noise signals. However, the non-coherent algorithms can track lower C/N₀ signals (i.e. SV2 and SV10) which means that the non-coherent algorithms have stronger robustness than coherent algorithms.

The position and velocity errors using different pre-filter algorithms are shown in figures 11 and 12, respectively. Tables 5 and 6 show the position and velocity error statistics, respectively. It is noted that the start epoch of figures 11 and 12

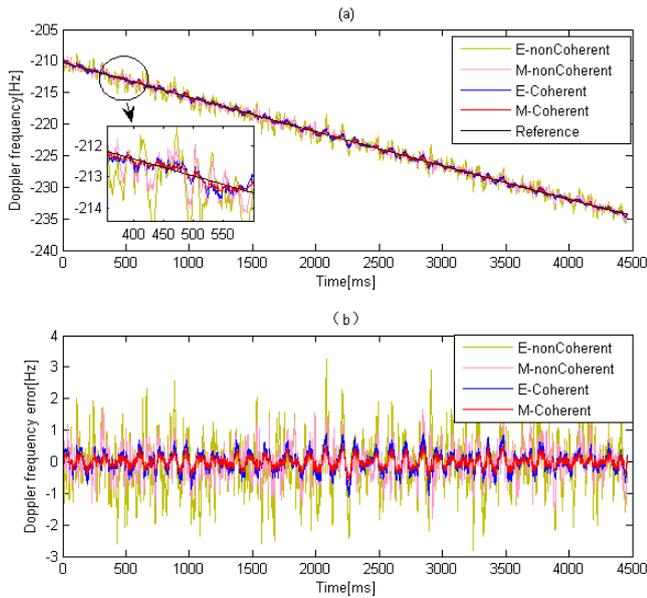


Figure 7. (a) Doppler frequencies of SV17 using different algorithms. (b) Doppler frequency errors of SV17 using different algorithms.

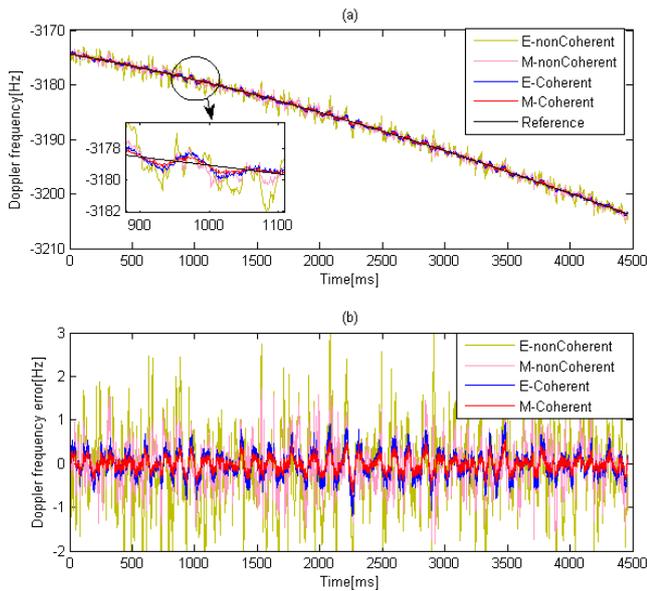


Figure 8. (a) Doppler frequencies of SV28 using different algorithms. (b) Doppler frequency errors of SV28 using different algorithms.

(also for figures 14, 18, 19 and 20) corresponds to the GPS time when the system starts to calculate the navigation solution.

The position error results shown in figure 11 and table 5 indicate that the position errors of the *M-Coherent* algorithm are reduced around 30%, 26% and 48% of the errors of the *E-Coherent* algorithm in east, north and up direction, respectively. The position errors of the *M-nonCoherent* algorithm are reduced around 10%, 2% and 22% of the errors of the *E-nonCoherent* algorithm in east, north and up direction, respectively. It can be seen that both of the coherent algorithms reach a better position accuracy than the non-coherent algorithms. Besides, all the coherent and non-coherent algorithms have a better position accuracy than the GNSS-only solution.

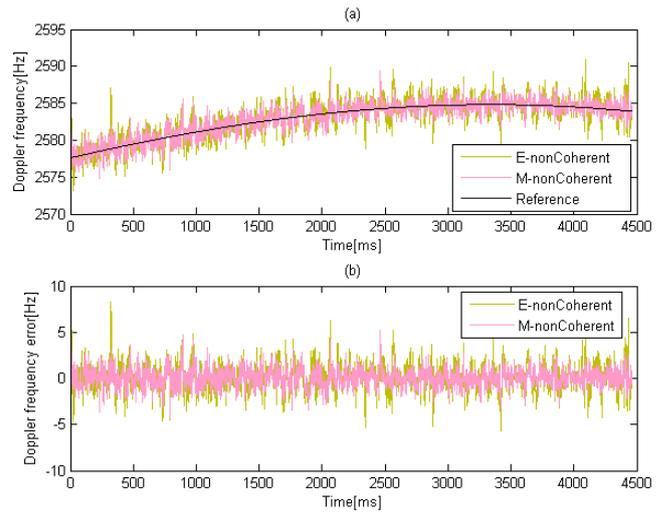


Figure 9. (a) Doppler frequencies of SV2 using different algorithms. (b) Doppler frequency errors of SV2 using different algorithms.

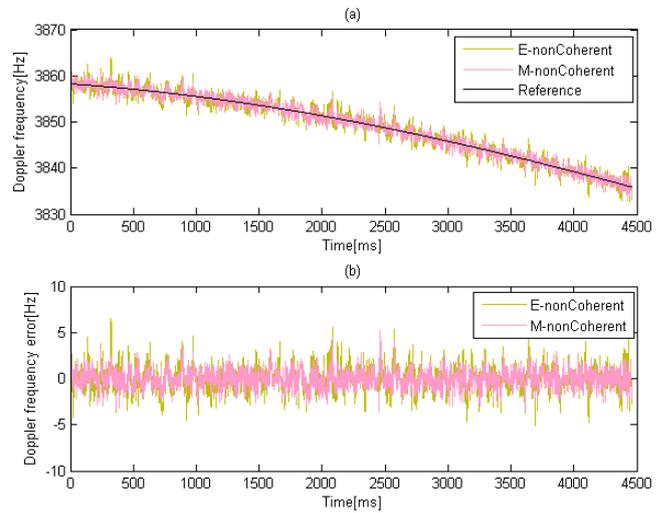


Figure 10. (a) Doppler frequencies of SV10 using different algorithms. (b) Doppler frequency errors of SV10 using different algorithms.

Table 4. Doppler frequency error statistics.

Pre-filter method	Doppler frequency error (RMS) for different satellites (Hz)			
	SV17	SV28	SV2	SV10
<i>E-Coherent</i>	0.2957	0.2978	/	/
<i>M-Coherent</i>	0.1700	0.1714	/	/
<i>E-nonCoherent</i>	0.8224	0.8746	1.4591	1.3523
<i>M-nonCoherent</i>	0.4771	0.4944	0.9996	0.9705

The velocity error results shown in figure 12 and table 6 indicate that the velocity errors of the *M-Coherent* algorithm are reduced around 45%, 46% and 39% of the errors of the *E-Coherent* algorithm in east, north and up direction, respectively. The velocity errors of the *M-nonCoherent* algorithm are reduced around 42%, 36% and 37% of the errors of the *E-nonCoherent* algorithm in east, north and up direction, respectively. It can be seen that both the coherent algorithms reach

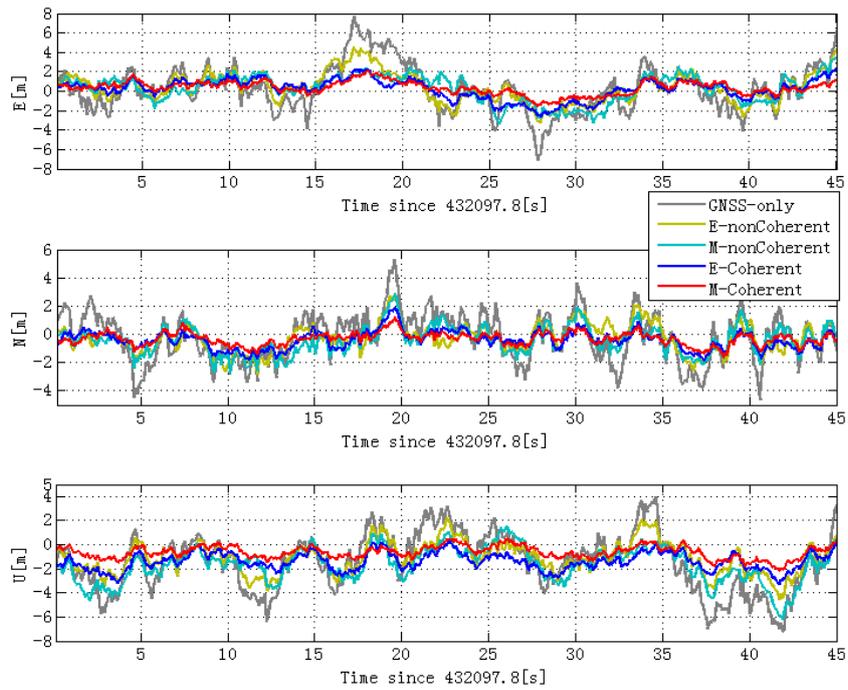


Figure 11. Position errors with simulator data.

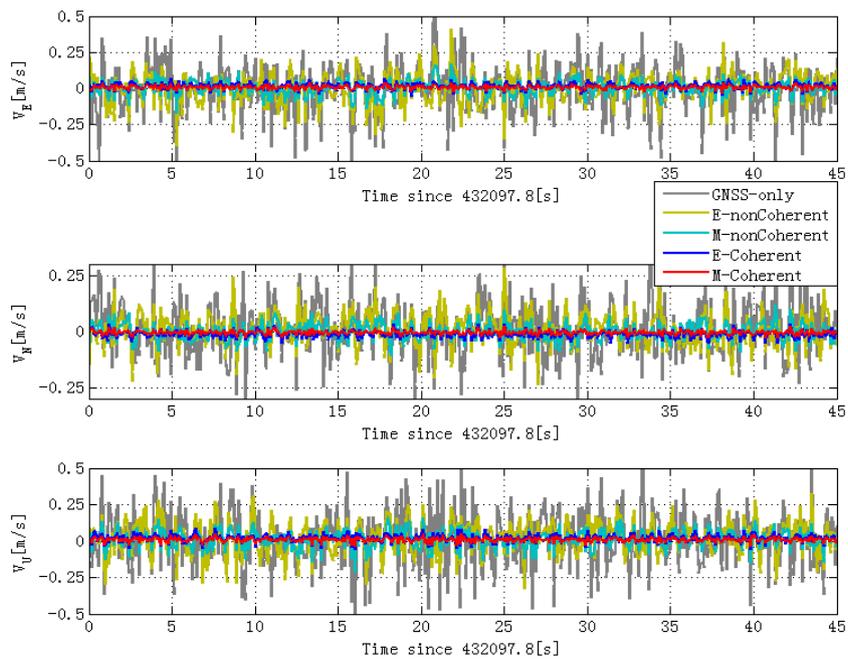


Figure 12. Velocity errors with simulator data.

a better velocity accuracy than the non-coherent algorithms. Besides, all the coherent and non-coherent algorithms have a better velocity accuracy than the GNSS-only solution.

The simulation test results indicate that the coherent algorithms can reach a better tracking and position accuracy while the non-coherent algorithms have a stronger robustness to track lower signal-to-noise signals. The proposed modified coherent and non-coherent algorithms (i.e. *M-Coherent* and *M-nonCoherent*) are proven improvements of both tracking and position performance compared to the existing

Table 5. RMS position error statistics.

Method	RMS position errors (m)		
	<i>E</i>	<i>N</i>	<i>U</i>
GNSS-only	2.39	1.73	2.79
<i>E-Coherent</i>	1.11	0.76	1.58
<i>M-Coherent</i>	0.78	0.57	0.82
<i>E-nonCoherent</i>	1.69	1.07	2.20
<i>M-nonCoherent</i>	1.52	1.04	1.71

Table 6. RMS velocity error statistics.

Method	RMS velocity errors (m s ⁻¹)		
	V_E	V_N	V_U
GNSS-only	0.181	0.125	0.196
<i>E</i> -Coherent	0.026	0.021	0.031
<i>M</i> -Coherent	0.015	0.011	0.019
<i>E</i> -nonCoherent	0.110	0.077	0.117
<i>M</i> -nonCoherent	0.064	0.049	0.073



Figure 13. The trajectory of the vehicle test.

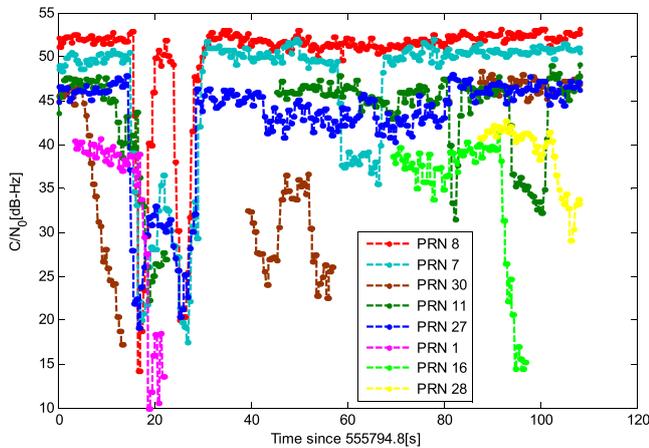


Figure 14. C/N_0 values of different satellites.

coherent and non-coherent algorithms (i.e. *E*-Coherent and *E*-nonCoherent).

4.2.2. Vehicle test. The vehicle test is conducted to compare the performance of the adaptive deeply-coupled system with hybrid pre-filters processing (Hybrid-DC), the single coherent deeply-coupled method (Coherent-DC) and the single non-coherent deeply-coupled method (nonCoherent-DC) under GNSS-challenged environment. The Hybrid-DC, Coherent-DC and nonCoherent-DC methods consist of the proposed modified coherent and non-coherent algorithms.

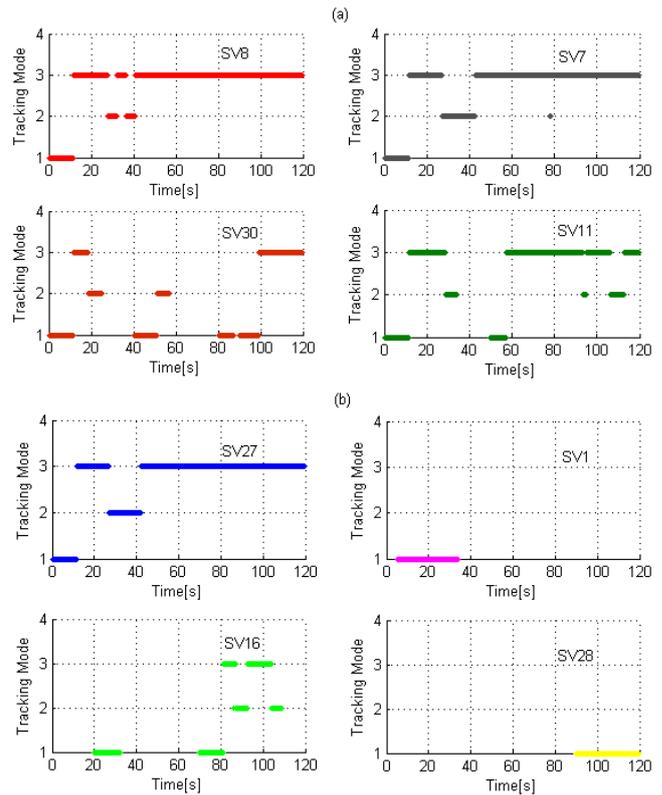


Figure 15. (a) and (b) The tracking modes for different satellites using the Hybrid-DC method.

Figure 13 shows the trajectory of the vehicle test. The car passes through the building, seen as a sheltered environment as shown in figure 13.

It can be seen in figure 14 that all C/N_0 values of the satellites decrease rapidly when the car passes through the building. During the pass time, almost all the satellites are blocked. After that, the signals recover gradually.

Figure 15 shows the tracking modes for different satellites using the Hybrid-DC method. The tracking mode of each channel switches automatically according to the signal quality to search for an optimal performance.

In figure 15, tracking mode 1 denotes the scalar traditional mode, 2 denotes the non-coherent mode and 3 denotes the coherent mode. It can be seen that the Hybrid-DC method works in hybrid mode, i.e. some of its channels work in coherent mode while others work in non-coherent mode. Note that the scalar traditional mode indicates that the channel just starts to track at the beginning or restarts tracking after re-acquisition.

The tracking information of I_P and Q_P for SV7 and SV27 are shown in figures 16 and 17. It can be seen that the signals are blocked at about 26s for both SV7 and SV27 when the car begins passing through the building. The channels are maintained mainly by the navigation feedback information (state 1). The channels using the Coherent-DC method lose lock at about 38s (state 2) and return to re-acquisition and re-tracking (state 3) at about 46s for SV7 and about 40s for SV27. However, the channels using the nonCoherent-DC and Hybrid-DC methods remain in state 1 until the car

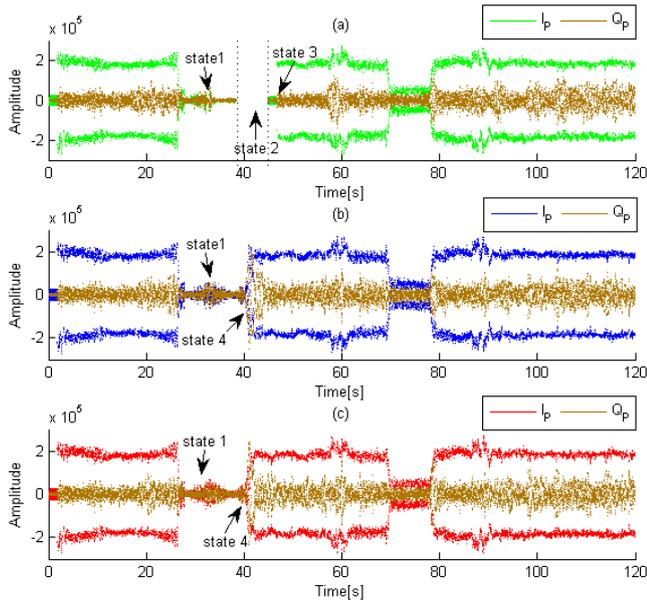


Figure 16. The tracking information of I_P and Q_P for SV7 using different method. (a) Coherent-DC. (b) nonCoherent-DC. (c) Hybrid-DC.

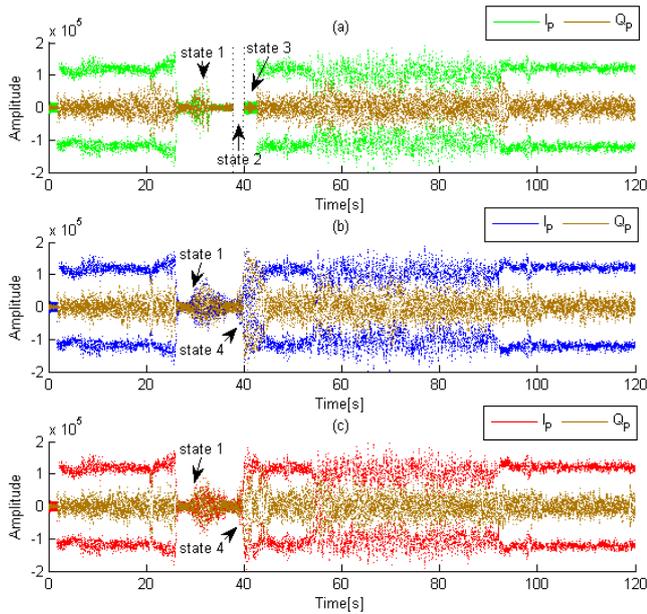


Figure 17. The tracking information of I_P and Q_P for SV27 using different method. (a) Coherent-DC. (b) nonCoherent-DC. (c) Hybrid-DC.

passes out of the building and recover tracking quickly (state 4). These results indicate that both of the nonCoherent-DC and Hybrid-DC methods have a stronger robustness for maintaining and recovering the blocked signal quickly.

Figure 18 shows the number of available satellites for different methods during the operating time. It can be seen that the proposed Hybrid-DC method can track the most number of satellites all the time. The nonCoherent-DC method also has a better tracking performance than the Coherent-DC method due to its better robustness.

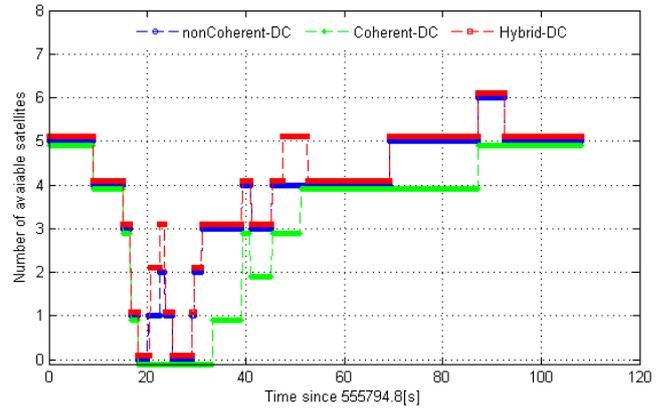


Figure 18. Number of available satellites.

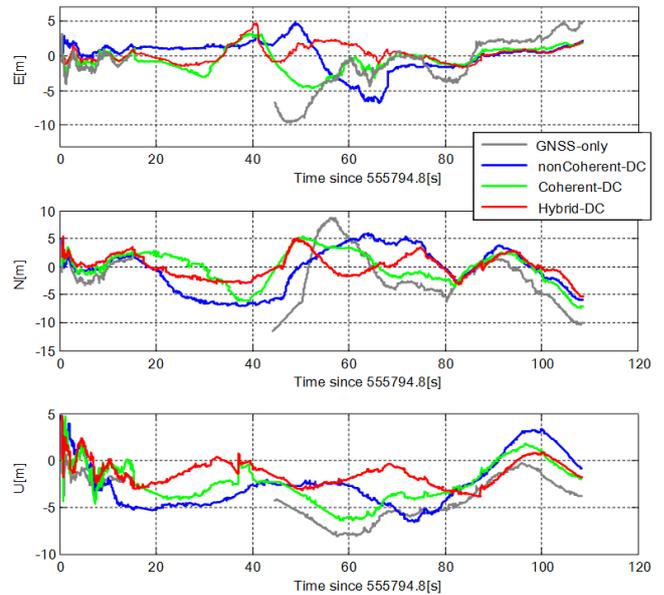


Figure 19. Position errors with vehicle data.

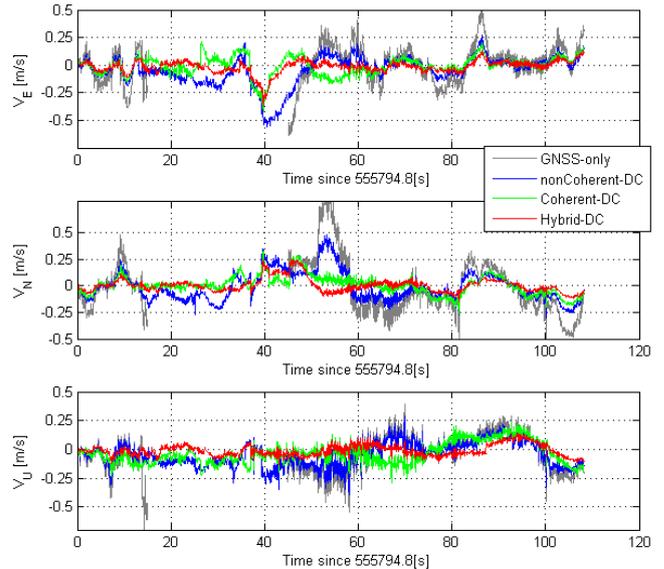


Figure 20. Velocity errors with vehicle data.

Table 7. RMS position error statistics.

Method	RMS position errors (m)		
	E	N	U
GNSS-only	3.44	4.83	4.16
Coherent-DC	2.17	3.61	3.03
nonCoherent-DC	2.73	4.36	3.56
Hybrid-DC	1.85	2.88	2.23

Table 8. RMS velocity error statistics.

Method	RMS velocity errors (m s^{-1})		
	V_E	V_N	V_U
GNSS-only	0.145	0.174	0.122
Coherent-DC	0.084	0.086	0.099
nonCoherent-DC	0.129	0.126	0.113
Hybrid-DC	0.076	0.074	0.069

The position and velocity errors using different methods are shown in figures 19 and 20, respectively. Tables 7 and 8 show the position and velocity error statistics, respectively.

The position error results shown in figure 19 and table 7 indicate that the position errors of the Hybrid-DC method are reduced around 15%, 20% and 26% of the errors of the Coherent-DC method and around 32%, 34% and 59% of the errors of the nonCoherent-DC method in east, north and up direction, respectively. Besides, all the coherent, non-coherent and hybrid algorithms have a better position accuracy than the GNSS-only solution.

The velocity error results shown in figure 20 and table 8 indicate that the velocity errors of Hybrid-DC method are reduced around 10%, 13% and 29% of the errors of the Coherent-DC method and around 41%, 40% and 37% of the errors of the nonCoherent-DC method in east, north and up direction, respectively. Besides, all the coherent, non-coherent and hybrid algorithms have a better velocity accuracy than the GNSS-only solution.

The vehicle results indicate that the proposed Hybrid-DC method reaches an optimal tracking and navigation performance by combining the advantages of the coherent and non-coherent algorithms. In the test, the robustness of the non-coherent mode enables the Hybrid-DC method to track more satellites especially in a GNSS-challenged environment. Meanwhile, the coherent mode helps the Hybrid-DC method to reach a better accuracy.

5. Conclusions and future work

The existing pre-filters of the deeply-coupled structures are modified and the improvement of the tracking performance are proved by the simulation test. An adaptive deeply-coupled GNSS/INS navigation system with hybrid pre-filters processing is proposed to combine the advantages of the coherent and non-coherent algorithms. The vehicle test results show that the proposed system can achieve accuracy and robustness performance preferably under a GNSS-challenged environment,

compared to the single coherent and non-coherent deeply-coupled method.

Note that only the GPS constellation and L1 CA signal are designed and simulated in the presented system, other GNSS constellations (such as Beidou, GLONASS and Galileo) can be included in the future work to realize joint tracking and navigation so as to reach a better performance.

Acknowledgment

This work was co-funded by the National Nature Science Foundation of China under grant No. 61633008, 61304234 and 61773132. The authors would like to thank all the editors and anonymous reviewers for improving this article.

ORCID iDs

Mouyan Wu  <https://orcid.org/0000-0002-7244-5776>

References

- [1] O'Driscoll C and Lachapelle G 2009 Comparison of traditional and Kalman filter based tracking architectures *Proc. of European navigation Conf.* pp 1–10
- [2] Kaplan E D and Hegarty C J 2006 *Augmented GPS: Principles and Applications* (Boston, MA: Artech House Publisher)
- [3] Chen W, Li X, Song X, Li B, Song X H and Xu Q M 2015 A novel fusion methodology to bridge GPS outages for land vehicle positioning *Meas. Sci. Technol.* **26** 075001
- [4] Aggarwal P, Syed Z and Elsheimy N 2009 Hybrid extended particle filter (HEPF) for integrated inertial navigation and global positioning systems *Meas. Sci. Technol.* **20** 055203
- [5] Han H Z and Wang J 2017 Robust GPS/BDS/INS tightly coupled integration with atmospheric constraints for long-range kinematic positioning *GPS Solut.* **21** 1285–99
- [6] Wang D J, Lv H F and Wu J 2017 Augmented Cubature Kalman filter for nonlinear RTK/MIMU integrated navigation with non-additive noise *Measurement* **97** 111–25
- [7] Zeng Q H, Meng Q, Liu J Y, Feng S J and Wang H H 2016 Acquisition and loop control of ultra-tight INS/BeiDou integration system *Optik* **127** 8082–9
- [8] Kou Y H and Zhang H 2016 Sample-wise aiding in GPS/INS ultra-tight integration for high-dynamic, high-precision tracking *Sensors* **16** 519
- [9] Yu J and Chen X Y 2010 Application of extended Kalman filter in ultra-tight GPS/INS integration based on GPS software receiver *Int. Conf. Green Circuits Syst., ICGCS (Shanghai, China, 21–23 June 2010)* pp 82–6
- [10] Xie F, Liu J Y, Li R B, Jiang B and Qiao L 2015 Performance analysis of a federated ultra-tight global positioning system/inertial navigation system integration algorithm in high dynamic environments *Proc. Inst. Mech. Eng. G* **229** 56–71
- [11] Ban Y L, Niu X J, Zhang T S, Zhang Q, Guo W F and Zhang H P 2014 Low-end MEMS IMU can contribute in GPS/INS deep integration *Recreation IEEE PLANS Position Location and Navigation Symp.* pp 746–52
- [12] Zhang T S, Zhang H P, Ban Y L, Yan K L, Niu X J and Liu J N 2015 Hardware implementation of a real-time MEMS IMU/GNSS deeply-coupled system *IEICE Trans. Commun.* **E96.B** 2933–42
- [13] Lashley M, Bevely D M and Hung J Y 2010 Analysis of deeply integrated and tightly coupled architectures *Recreation*

- IEEE PLANS Position Location Navigation Symp.* pp 382–96
- [14] Petovello M G and Lachapelle G 2006 Comparison of vector-based software receiver implementations with application to ultra-tight GPS/INS integration *Proc. Institute Navigation Int. Technical Meeting Satellite Division ION GNSS (Fort Worth, TX, USA, 26–29 September 2006)* pp 1790–9
- [15] Wang X L, Li Y F and Ji X C 2015 *Techonology of SINS/GPS Integrated Navigation* (Beijing: Beihang University Press)
- [16] Groves P D 2013 *Principles of GNSS, Inertial, and Multisensor Integrated Navigation Systems* (Boston, MA: Artech House Publisher)
- [17] Niu X J, Ban Y L, Zhang T S and Liu J N 2016 Research progress and prospects of GNSS/INS deep integration *Acta Aeronaut. Astronaut. Sin.* **37** 2859–908
- [18] Groves P D, Mather C J and Macaulay A A 2007 Demonstration of non-coherent deep INS/GPS integration for optimized signal-to-noise performance *Proc. Int. Technical Meeting of the Satellite Division Institute of the Navigation, ION GNSS (Fort Worth, TX, USA, 25–28 September 2007)* pp 2627–38
- [19] Psiaki M L 2001 Smoother-based GPS signal tracking in a software receiver *Int. Technical Meeting of the Satellite Division Institute of the Navigation, ION GPS (Salt Lake, UT, USA, 11–14 September 2001)* pp 2990–13
- [20] Psiaki M L and Jung H 2002 Extended Kalman filter methods for tracking weak GPS signals *Int. Technical Meeting of the Satellite Division Institute of the Navigation, ION GPS (Salt Lake, UT, USA, 24–27 September 2002)* pp 2539–53
- [21] Fonville B, Powers E and Matsakis D 2013 Determination of early-late discriminator errors on filtered BPSK waveforms *Proc. Institute of the Navigation Int. Technical Meeting of the Satellite Division ION GNSS (Fort Worth, TX, USA, 16–20 September 2013)* pp 3600–6
- [22] Izadpanah A 2009 *Parameterization of GPS L1 multipath using a dual polarized RHCP/LHCP antenna* (Calgary: Department of Geomatics Engineering, University of Calgary)
- [23] Luo Z B, Ding J C, Zhao L and Wu M Y 2017 The code phase error compensation technique in GNSS receivers *Proc. Int. Meeting Institute Navigation, ION ITM (Monterey, CA, USA, 30 January–2 February 2017)* pp 365–87
- [24] Arasaratnam I and Haykin S 2009 Cubature Kalman filters *IEEE Trans. Autom. Control* **54** 1254–69
- [25] Jia B, Xin M and Cheng Y 2013 High-degree cubature Kalman filter *Automatica* **49** 510–18
- [26] Luo Y, Babu R, Wu W Q and He X F 2012 Double-filter model with modified Kalman filter for baseband signal pre-processing with application to ultra-tight GPS/INS integration *GPS Solut.* **16** 463–76
- [27] Balaei A T, Dempster A G and Barnes J 2006 A novel approach in detection and characterization of CW interference of GPS signal using receiver estimation of C/N_0 *Recreation IEEE PLANS Position Location Navigation Symp. (San Diego, CA, USA, 25–27 April 2006)* pp 1120–6